



OPEN

Grain-size-evolution controls on lithospheric weakening during continental rifting

J. B. Ruh  , L. Tokle and W. M. Behr

Variation in the effective strength of the lithosphere allows for active plate tectonics and is permitted by different deformation mechanisms operating in the crust and upper mantle. The dominant mechanisms are debated, but geodynamic models often employ grain-size-independent mechanisms or evaluate a single grain size. However, observations from nature and rock deformation experiments suggest a transition to grain-size-dependent mechanisms due to a reduction in grain size can cause lithospheric weakening. Here, we employ a two-dimensional thermo-mechanical numerical model of the upper mantle to investigate the nature of deformation and grain-size evolution in a continental rift setting, on the basis of a recent growth law for polycrystalline olivine. We find that the average olivine grain size is greater in the asthenospheric mantle (centimetre-scale grains) than at the crust-mantle boundary (millimetre-scale grains). This grain-size distribution could result in dislocation creep being the dominant deformation mechanism in the upper mantle. However, we suggest that along lithospheric-scale shear zones, a reduction in grain sizes due to localized deformation causes a transition to diffusion creep as the dominant deformation mechanism, causing weakening of the lithosphere and facilitating the initiation of continental rifting.

The Earth's lithosphere is defined by its mechanically rigid behaviour in contrast to the relatively weak underlying asthenosphere. This rheological stratification, which ultimately allowed for the emergence of plate tectonics, results primarily from the thermal gradient across the crust and upper mantle and the temperature-dependent activation of dislocation- and diffusion-related crystal-plastic creep of rocks and minerals^{1–4}. Scaling of such experimentally derived creep laws to natural strain rates allows us to estimate viscosities and strength of the lithosphere (Extended Data Fig. 1). Geophysical constraints on the elastic thickness of the continental lithosphere, which is a proxy for its strength, led to contrasting views on the strength of the uppermost mantle, with it being either strong and best represented by dry dislocation creep of olivine⁵ or weak according to a wet olivine rheology^{6,7}.

Whether deformation within the upper mantle is dominated by dislocation creep or diffusion creep is still a matter of debate. The observation of crystallographic preferred orientation in mantle xenoliths⁸ and evidence for strong seismic anisotropy⁹ has long been interpreted as an indicator for dislocation creep as the dominant deformation mechanism¹⁰. However, there is reported evidence that crystallographic preferred orientation, and therefore seismic anisotropy, may also develop as a result of diffusion creep of fine-grained olivine-rich aggregates¹¹. In contrast to dislocation creep, the relationship between stress and strain rate for diffusion creep is dependent on grain size, which is a crucial parameter when considering the dominant deformation mechanism in the upper mantle^{1,3,12}. A transition from dislocation to diffusion creep at depths greater than ~250 km was proposed by Hirth and Kohlstedt¹ on the basis of theoretical estimates that olivine grain size in the upper mantle is on the order of 10 mm¹³. Numerical experiments of mantle convection have since implemented a composite diffusion–dislocation creep rheology and constant mantle grain size, which may result in dramatic convective instability and thermal erosion of the lithosphere¹⁴. However, the assumption of a constant upper-mantle grain size is an oversimplification that appears contradictory to several observational and experimental datasets. Experimental data on

wave speed and attenuation of olivine, for example, fit best with a seismological model that implies an increase in grain size from ~1 mm to ~5 cm between depths of 100 and 200 km¹⁵. Furthermore, natural samples of exhumed lithospheric mantle rocks show a large variety of grain sizes ranging from tens to hundreds of microns in olivine mylonites and tectonites to the centimetre scale in weakly deformed or annealed xenoliths^{16–18}.

Plate tectonics requires mechanical weakening and prolonged strain localization along lithospheric shear zones at the plate boundaries^{19,20}. Several studies suggest that grain-size reduction and the consequent activation of diffusion creep is a viable process to initiate localization of deformation in the lithosphere^{21–25}, perhaps complementary to other potential weakening mechanisms such as shear heating²⁶, reaction-induced weakening²⁷ or the presence of pre-existing weak zones or viscous anisotropy²⁸. For example, Bercovici and Ricard^{29,30} demonstrated that dynamic grain damage and phase mixing may explain fast (<1 Myr) weakening and localization of shear zones because Zener pinning severely inhibits the process of grain growth. By contrast, long-term grain-size-dependent weakening in the absence of grain pinning has been considered unlikely³¹ due to fast grain-growth laws for olivine³². Unfortunately, most models that investigate grain-size-related weakening describe one-dimensional parameterizations that lack the necessary dynamic context to better understand complex tectonic systems^{21,33,34}. Furthermore, recent studies suggest that the coupling of grain size and thermo-mechanical systems has important effects on the dynamics of mantle convection³⁵, the initiation of transfer faults²⁵ and the segmentation of subducting slabs³⁶.

In this Article, we present a two-dimensional thermo-mechanical numerical model with a composite diffusion–dislocation creep flow law coupled to a self-consistent grain-size-evolution model based on the palaeowattmeter³⁷. Such a model allows us to estimate apparent grain-size distribution and the dominant deformation mechanism within the upper mantle and to investigate the importance of grain-size evolution for strain localization in the lithosphere during continental rifting. The two-dimensional approach furthermore

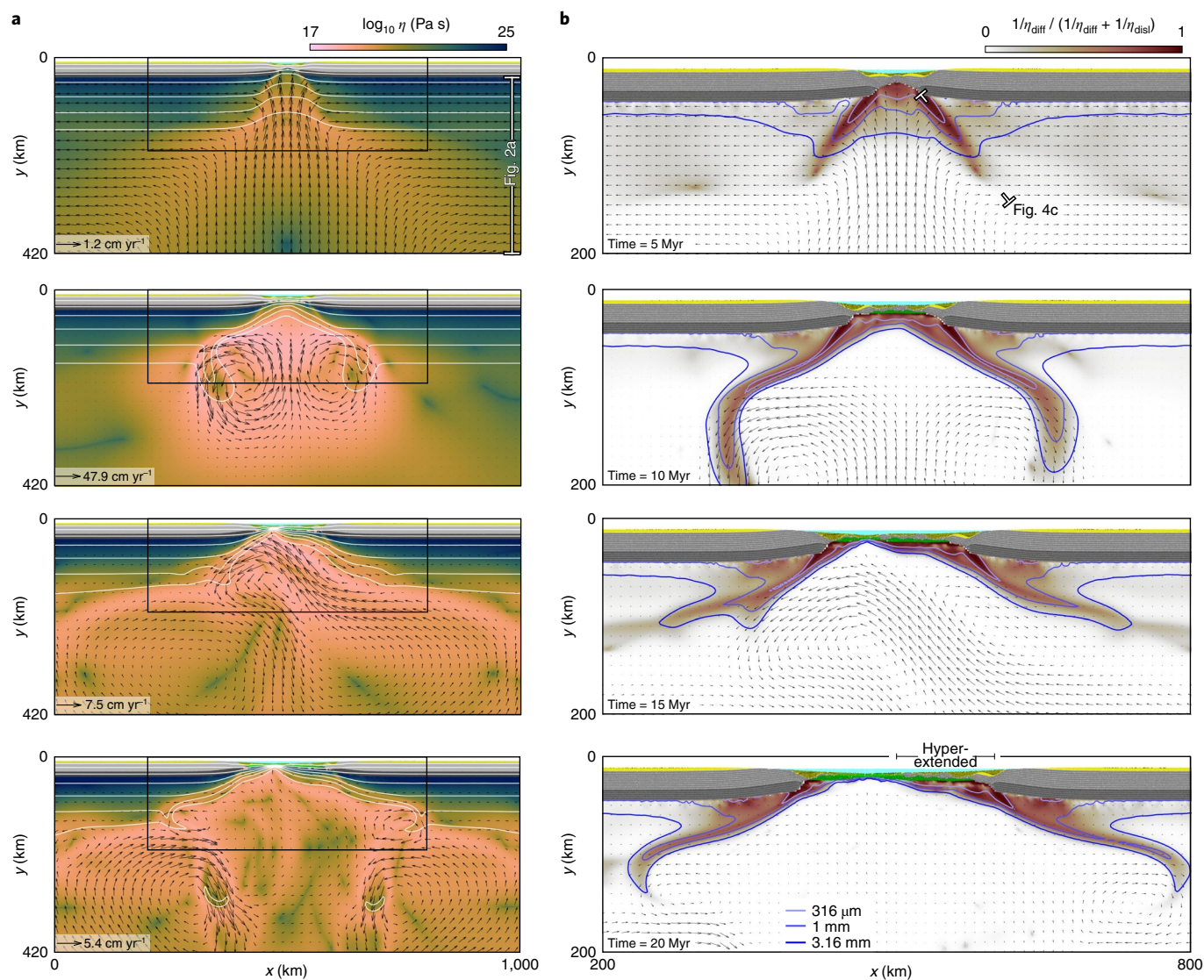


Fig. 1 | Temporal evolution of the experiment with $C_{OH} = 600 \text{ H}/10^6 \text{ Si}$. **a**, Viscosity of upper mantle and marker composition of crust. White lines denote isotherms up to $1,300^\circ\text{C}$. **b**, Deformation mechanism in the uppermost mantle and composition of crust. Red, diffusion creep; white, dislocation creep; blue contours indicate grain size; grey and yellow colours, continental crust marker composition; green, oceanic crust marker composition; x, width; y, depth.

allows for the evaluation of complex thermal and geometric feedback effects related to upper-mantle dynamics. We test the influence of hydrogen concentration in the mantle, which affects both its viscosity and rate of grain growth. Furthermore, the effect of localized grain-size-dependent weakening on the long-term strength and elastic thickness of continental lithosphere is investigated and compared with pure dislocation-creep experiments.

Modelling grain-size evolution in the upper mantle

We apply a finite-difference thermo-mechanical numerical model of the upper mantle and crust with a Eulerian domain of $1,000 \times 670 \text{ km}$ that undergoes horizontal divergence at a constant total rate of 1 cm yr^{-1} (Extended Data Fig. 2). Additional experiments were run with divergence rates of 4 and 8 cm yr^{-1} for comparison. The model employs a visco-elasto-plastic rheology where the viscous strain rate is composed of both dislocation and diffusion creep for a constant hydrogen concentration¹ and stresses are capped depending on the Drucker–Prager yield criterion (Extended Data Tables 1–3 and Methods). Although grain boundary sliding (GBS) may be important in olivine at dry conditions³⁸, it is expected

to have a minor effect in wet experiments¹, requiring either high stresses ($>1 \text{ GPa}$) or high temperatures ($>1,500^\circ\text{C}$) for grain sizes of 1–10 mm (ref. 39). Nevertheless, we conducted additional experiments including a wet GBS flow law³⁹ to test its effect on the mechanics of the upper mantle. The applied hydrogen concentrations in the mantle are $C_{OH} = 50, 175, 600$ and $2,500 \text{ H atoms per } 10^6 \text{ Si atoms (H}/10^6 \text{ Si)}$, which cover the range of estimated values obtained from experimental studies^{40,41}, and measured values from mid-ocean ridge basalts⁴², and peridotite xenoliths⁴³ (Methods). Olivine grain size is calculated on the basis of the palaeo-wattmeter³⁷, which introduces a grain-size-evolution rate composed of independent growth and reduction terms (Extended Data Table 4 and Methods). Grain-size reduction occurs through the process of dynamic recrystallization during dislocation creep, whereas grain growth controls the grain size during diffusion creep⁴⁴. Therefore, only dislocation creep is responsible for grain-size reduction. On the basis of grain sizes from experimentally deformed olivine aggregates, the fraction of work that goes into grain-size reduction during dynamic recrystallization is estimated to be $\lambda = 0.01$ (Extended Data Fig. 3a), which is in agreement with recent estimates for olivine⁴⁵.

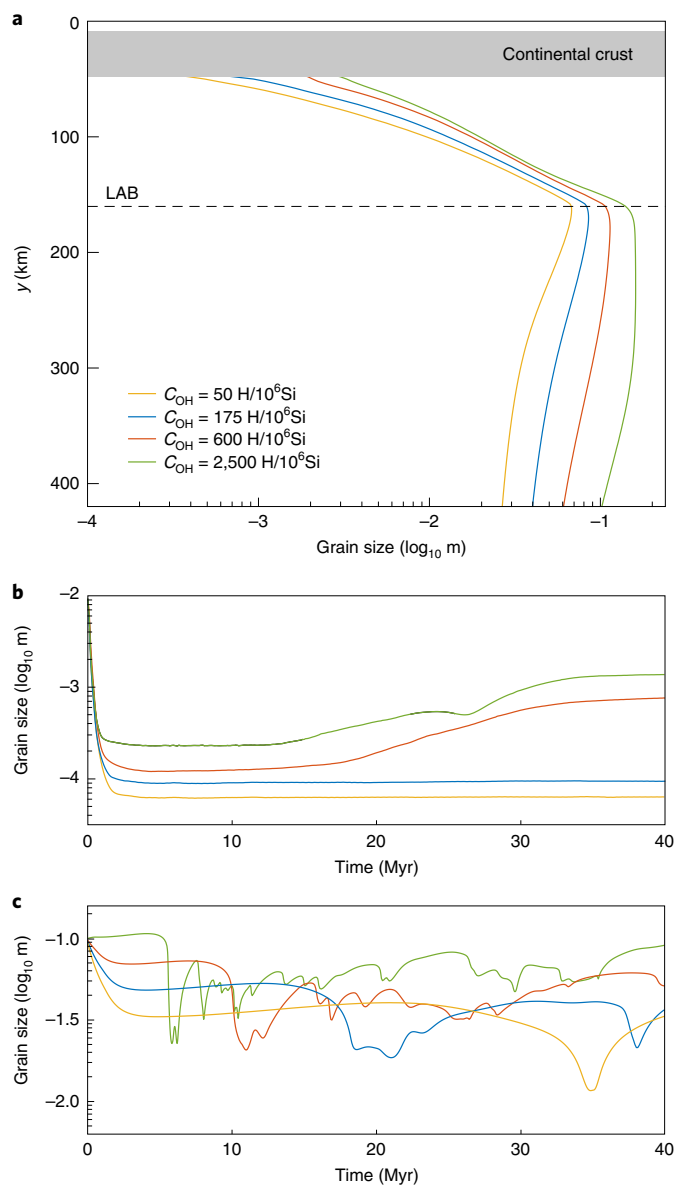


Fig. 2 | Grain sizes in the mantle at variable water content. **a**, Vertical profile at $x = 990$ km after 5 Myr. See location in Fig. 1a. **b**, Temporal evolution of grain size within lithospheric shear zones at $y = 50$ km. **c**, Temporal evolution of grain size between 200 and 410 km depth.

Additional experiments were conducted with $\lambda = 0.003$, 0.04 and 0.1 for comparison. The implemented grain-growth parameters derive from experiments on natural olivine aggregates with in situ hydrogen concentrations⁴⁶ that predict substantially slower grain growth than previous constraints from experiments on water-saturated, synthetic olivine³² (Extended Data Fig. 3b). Grain sizes within the lithosphere are driven mainly by the reduction term due to lower temperatures and higher deviatoric stresses (Extended Data Fig. 3c). However, initial grain sizes in the lower part of the model domain rapidly adjust to a steady-state grain size due to high temperatures and thus fast growth rates (Extended Data Fig. 3d),.

Rheological implications and the formation of shear zones

Composite diffusion–dislocation-creep numerical experiments were conducted with various constant hydrogen concentrations in the mantle ($C_{\text{OH}} = 50, 175, 600$ and $2,500$ H/10⁶ Si) that affect both viscous creep and grain growth. Mantle viscosities of the reference

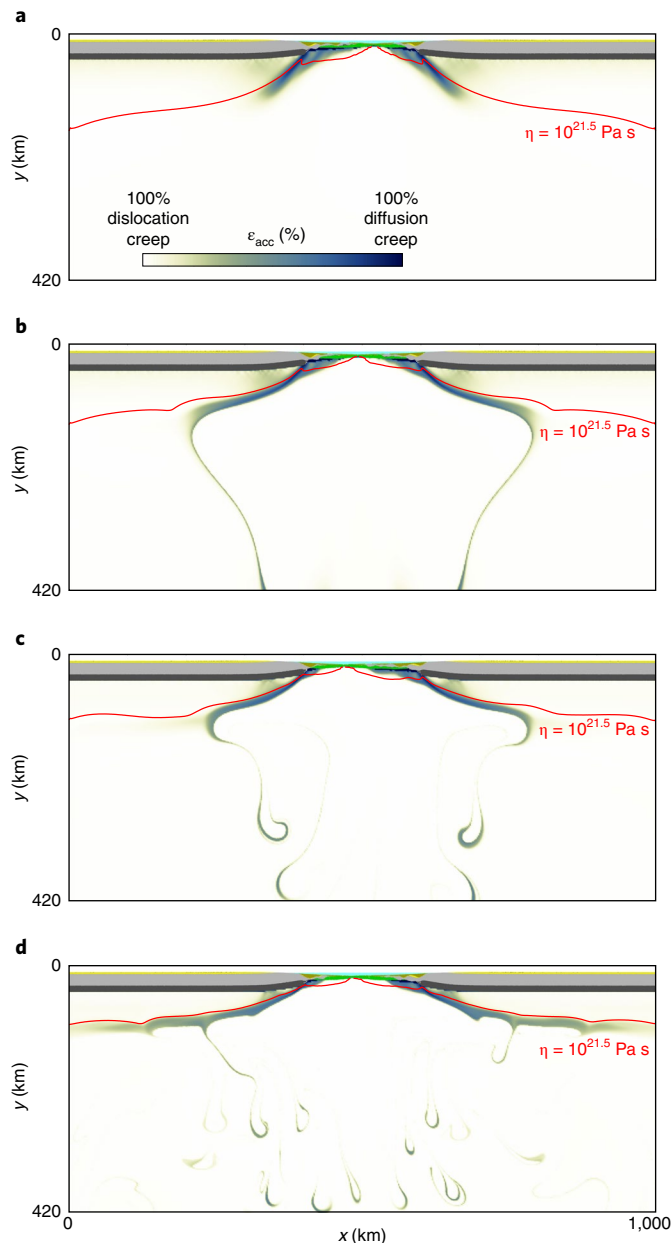


Fig. 3 | Percentage of finite strain accumulation in a lithospheric shear zone. Strain due to diffusion creep (blue) or dislocation creep (white) after 20 Myr of divergence. Red, contour of $\eta = 10^{21.5}$ Pa s indicating thickness of the elastic lithosphere. **a**, $C_{\text{OH}} = 50$ H/10⁶ Si. **b**, $C_{\text{OH}} = 175$ H/10⁶ Si. **c**, $C_{\text{OH}} = 600$ H/10⁶ Si. **d**, $C_{\text{OH}} = 2,500$ H/10⁶ Si.

model ($C_{\text{OH}} = 600$ H/10⁶ Si) show values of 10^{19} – 10^{21} Pa s for the asthenosphere after 5 Myr of divergence (Fig. 1a). At 10 Myr, lithospheric thinning and related temperature increase below the rifted region lead to viscosities as low as 5×10^{17} Pa s, relatively fast velocities and gravitationally induced lithospheric dripping. After 15 and 20 Myr of divergence, asthenospheric viscosities remain within 10^{18} – 10^{21} Pa s, with lower values where fast velocities occur due to thermally and gravitationally induced lithospheric erosion (Fig. 1a). Away from the rift, the lithosphere remains intact and strong. Additional experiments including GBS deformation mechanism³⁹ with hydrogen concentrations of $C_{\text{OH}} = 50$ H/10⁶ Si indicate a negligible and for $C_{\text{OH}} = 600$ H/10⁶ Si a minor (<1% of total strain rate) contribution of GBS to upper-mantle dynamics (Extended Data Fig. 4).

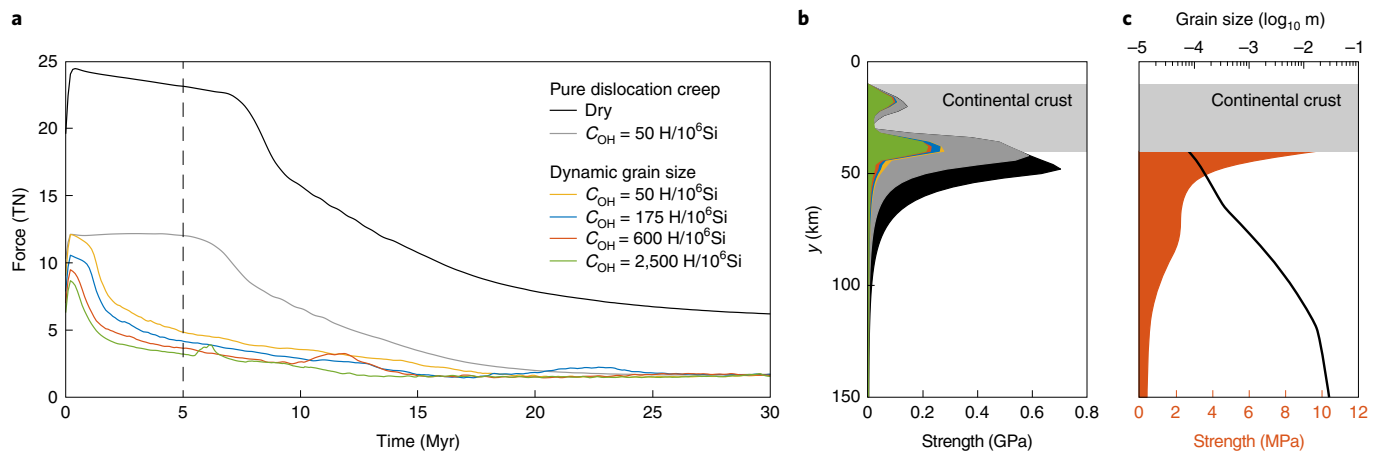


Fig. 4 | Strength of the lithosphere. **a**, Temporal evolution of the laterally averaged integrated strength (boundary force) of pure dislocation and grain-size-dependent composite diffusion–dislocation–creep experiments. **b**, Laterally ($x=990$ – $1,000$ km) averaged lithospheric strength profiles after 5 Myr. For colour code, see **a**. **c**, Strength and grain-size profile along lithospheric shear zone at 5 Myr. Location of profile indicated in Fig. 1b.

Illustrations of the dominant deformation mechanism (dislocation versus diffusion creep) and contours of grain size in the mantle demonstrate that localization of stress in the centre of the model domain leads to grain-size reduction and the activation of diffusion creep along large-scale lithospheric shear zones (Fig. 1b). The large shear zones retain relatively small grain sizes and remain dominated by diffusion creep even after 15 to 20 Myr of divergence, when a mid-ocean spreading centre is established, consuming most of the extensional velocity. This general observation is also valid if the fraction of work that goes into grain-size reduction is varied to $\lambda=0.004$, 0.03 and 0.1, with larger λ values resulting in smaller grain sizes and a stronger impact of diffusion creep within the mantle lithosphere (Extended Data Fig. 5a–c). In contrast to the grain-growth law for natural damp olivine aggregates, the implementation of much faster grain-growth law from water-saturated synthetic olivine³² results in grain sizes responsible for dislocation creep dominating across the entire upper mantle and the lack of grain-size-induced weakening (Extended Data Fig. 5d). This result has previously led to the suggestion that phase mixing and grain boundary pinning is the primary driver for strain localization in mantle shear zones²⁹. However, our results demonstrate that even in the absence of phase mixing, grain growth is sluggish enough to permit sustained localization through the persistence of diffusion creep after initial dynamic recrystallization. This result is consistent with observations from nature that many mantle shear zones also localize in olivine-dominated (for example, non-phase-mixed) peridotites such as dunites^{18,47}.

For experiments with the recent grain-growth law and a $\lambda=0.01$, grain sizes vary spatially throughout the model domain; furthermore, their values are strongly sensitive to implemented mantle hydrogen concentration. Vertical grain-size profiles along the side of the domain (at 5 Myr), away from the extensional zone, show values of 0.3–3.0 mm at the Moho (depending on C_{OH}) that increase to 6–15 cm at the lithosphere–asthenosphere boundary (LAB) and decrease to 3–10 cm at the base of the olivine-rich mantle at 410 km depth (Fig. 2a). Grain sizes within localizing shear zones in the uppermost lithosphere at 40 km depth ($y=50$ km) show a rapid initial decrease to 60–250 μm (Fig. 2b). Depending on the hydrogen concentration in the mantle, they are able to recover after ~ 15 Myr ($C_{\text{OH}}=2,500$ H/10⁶ Si) or ~ 20 Myr ($C_{\text{OH}}=600$ H/10⁶ Si). Lower hydrogen concentration hampers substantial grain growth within previously active shear zones before 40 Myr. Average upper-mantle grain sizes below 300 km depth establish within ~ 2 Myr and range between 3 and 12 cm (Fig. 2c). Further undulations in average

mantle grain size result from the downwelling of small-grain-size lithospheric driplets.

Figure 3 shows the portions of accumulated finite viscous strain within the mantle accommodated by diffusion and dislocation creep after 20 Myr of divergence. Dislocation creep is the dominant deformation mechanism in large parts of the upper mantle, independent of hydrogen concentration. Diffusion creep dominates within lithospheric shear zones that form in the early stages of rifting (Fig. 1b) and assist in lithospheric dripping (Fig. 3b–d). The continental lithospheric thickness defined by its viscosity varies between 90 and 150 km, depending on hydrogen concentration (Fig. 3).

Effects of grain size on lithospheric strength

The importance of a self-consistent grain-size distribution for upper-mantle dynamics becomes evident when comparing our results with numerical experiments with pure dislocation creep of olivine or composite diffusion–dislocation creep with a constant grain size throughout the entire upper mantle. Experiments with dry dislocation creep result in a thicker elastic lithosphere and increased viscosities (Extended Data Fig. 6a). Experiments with composite diffusion–dislocation creep and small constant grain size (1 mm) result in a lithosphere thinned by convective erosion (<90 km) driven by low asthenosphere viscosities of $<10^{18}$ Pa s (Extended Data Fig. 6b). For constant grain sizes larger than 1 cm, dislocation creep becomes the main deformation mechanism throughout the entire upper mantle¹⁴. These numerical experiments fail to match the effective elastic lithospheric thicknesses necessary to sustain orogens⁵, while brittle deformation in the lithosphere remains absent⁷. However, our implementation of a self-consistent grain-size evolution is able to resolve this obstacle. Observed lithospheric thicknesses vary between 90 and 150 km (Fig. 3), while localization of deformation in the mantle lithosphere rapidly leads to grain-size reduction, diffusion-creep activation and related stress drop below the frictional yield, omitting failure. The diffusion-creep-related stress drop furthermore reduces and replaces the importance of (work-related) shear heating along lithospheric shear zones^{26,48}.

The temporal evolution of the vertically integrated strength illustrates that experiments with composite diffusion–dislocation creep coupled to a self-consistent grain-size evolution show a decrease of boundary forces below 5 TN m⁻¹ within 1–2 Myr, while pure dislocation-creep experiments remain above 10 TN m⁻¹ for at least ~ 15 Myr (Fig. 4a). Typical forces along plate boundaries are on the order of 1–5 TN m⁻¹ (refs. 49,50), which is sufficient to

initiate continental rifting if the grain size is small enough and diffusion creep dominates deformation²³. Vertical strength profiles indicate that most of the strength of coupled experiments remains within the crust, with maximal values of ~200 MPa, while pure dislocation-creep experiments exhibit at least 10 km of brittle-plastic mantle lithosphere with differential stresses up to ~600–700 MPa (Fig. 4b). Differential stresses of ~200 MPa close to the Moho in composite diffusion-dislocation-creep experiments stand in contrast to significantly lower strength along a lithospheric shear zone after 5 Myr (Fig. 4c). There, values of 1–10 MPa are defined by grain sizes as small as 100 µm and diffusion creep as the consequent deformation mechanism, efficiently weakening the entire lithospheric rift system.

Hydrogen concentration in the upper mantle has important implications for the relationships between viscous flow and seismic anisotropy⁴¹, hydrous melting⁵¹ and the distribution of geochemical reservoirs⁵². The strength of olivine in the presence of water is significantly reduced^{53,54}, as expressed in the flow law we apply¹. Furthermore, increased hydrogen concentration results in faster olivine grain growth⁴⁶. The combined increase in grain-growth rate and decrease in flow stress associated with higher hydrogen concentrations in our experiments leads to lower asthenospheric viscosity and increased thermal erosion of the lithosphere driven by diffusion creep (Fig. 3).

The numerically predicted olivine grain size in the upper lithosphere away from shear zones (0.5–10 mm; Fig. 2a) is in agreement with naturally measured values from exhumed xenoliths^{16,55,56}. Furthermore, recrystallized grain sizes of 10–100 µm from localized lithospheric shear zones^{57–59} match the grain sizes established in the diffusion-creep-dominated numerical shear zones for hydrogen concentrations >175 H/10⁶ Si (Fig. 2b). There are only a few constraints on grain size in the lower part of the upper mantle. However, Faul and Jackson¹⁵ suggested that the seismic signature of the upper-mantle low-velocity zone may be explained with a grain size of 5 cm together with the presence of fluids, which is consistent with our numerical results (Fig. 2a,b).

Implications for continental margin architecture

Numerical experiments with a self-consistent grain-size-evolution model result in reduced grain sizes and the consequent activation of diffusion creep below continental rift zones. The long-term low viscosity of such lithospheric shear zones leads to mechanical decoupling along the Moho and allows for stretching of the continental crust and the formation of a hyper-extended margin, where the continental crust is <10 km thick horizontally extended over >100 km with a lack of high-angle faulting⁶⁰, forming continental slivers and extensional allochthons⁶¹ (Fig. 1b). Previous studies demonstrated that strain-dependent rheologies (either brittle or viscous strain weakening) of continental crust and lithospheric mantle play a crucial role in the formation of asymmetric rifting and hyper-extended margins^{62,63}. In fact, numerical experiments with a pure dislocation-creep mantle flow and without a grain-size-dependent weakening consistently produce symmetric and localized rifts (Extended Data Fig. 6a). This is also the case for experiments with a constant grain size of 1 mm due to the strong, dislocation-creep-dominated uppermost mantle lithosphere (Extended Data Fig. 6b).

The formation of diffusion-creep-dominating mantle shear zones is also observed when increasing the divergence velocity of rifting experiments to a total of 4 and 8 cm yr⁻¹ (Extended Data Fig. 6c,d). However, faster extension leads to increased rifting symmetry, with smaller grain sizes in the mantle lithosphere. The impact of weak rheologies and plate velocities on rift architecture is not novel^{62–64}. However, in contrast to previous studies, we present a self-consistent fully coupled physical implementation supported by observed variance of grain size in mantle rocks that is responsible for

crust-mantle mechanical decoupling necessary to form hyper-extended margins.

In summary, presented numerical results are able to reproduce naturally observed distributions of olivine grain size, which indicate that dislocation creep is the dominant deformation mechanism in the upper mantle except along lithospheric shear zones, where diffusion creep is activated as a result of grain-size reduction by earlier dislocation creep at high stress. This intrinsic weakness of such shear zones reduces the necessary boundary force to initiate continental break-up and accelerates related rifting events. A typical feature of our experiments including grain-size evolution is the development of hyper-extended margin architectures, enabled by mechanical decoupling along diffusion-creep-dominated weaknesses below the extending continental crust.

Online content

Any methods, additional references, Nature Research reporting summaries, source data, extended data, supplementary information, acknowledgements, peer review information; details of author contributions and competing interests; and statements of data and code availability are available at <https://doi.org/10.1038/s41561-022-00964-9>.

Received: 26 May 2021; Accepted: 12 May 2022;

Published online: 16 June 2022

References

- Hirth, G. & Kohlstedt, D. in *Inside the Subduction Factory* (ed. Eiler, J.) 83–106 (AGU, 2003).
- Hirth, G., Teyssier, C. & Dunlap, W. J. An evaluation of quartzite flow laws based on comparisons between experimentally and naturally deformed rocks. *Int. J. Earth Sci.* **90**, 77–87 (2001).
- Karato, S. & Wu, P. Rheology of the upper mantle—a synthesis. *Science* **260**, 771–778 (1993).
- Rybacki, E. & Dresen, G. Dislocation and diffusion creep of synthetic anorthite aggregates. *J. Geophys. Res. Solid Earth* **105**, 26017–26036 (2000).
- Burov, E. B. & Watts, A. B. The long-term strength of continental lithosphere: ‘jelly sandwich’ or ‘crème brûlée’? *GSA Today* **16**, 4–10 (2006).
- Jackson, J. A. Strength of the continental lithosphere: time to abandon the jelly sandwich? *GSA Today* **12**, 4–10 (2002).
- Maggi, A., Jackson, J. A., McKenzie, D. & Priestley, K. Earthquake focal depths, effective elastic thickness, and the strength of the continental lithosphere. *Geology* **28**, 495–498 (2000).
- Jin, D. H., Karato, S. & Obata, M. Mechanisms of shear localization in the continental lithosphere: inference from the deformation microstructures of peridotites from the Ivrea zone, northwestern Italy. *J. Struct. Geol.* **20**, 195–209 (1998).
- Gung, Y. C., Panning, M. & Romanowicz, B. Global anisotropy and the thickness of continents. *Nature* **422**, 707–711 (2003).
- Karato, S. Rheology of the deep upper mantle and its implications for the preservation of the continental roots: a review. *Tectonophysics* **481**, 82–98 (2010).
- Miyazaki, T., Sueyoshi, K. & Hiraga, T. Olivine crystals align during diffusion creep of Earth’s upper mantle. *Nature* **502**, 321–326 (2013).
- Faul, U. H. & Jackson, I. Diffusion creep of dry, melt-free olivine. *J. Geophys. Res. Solid Earth* **112**, B04204 (2007).
- Evans, B., Renner, J. & Hirth, G. A few remarks on the kinetics of static grain growth in rocks. *Int. J. Earth Sci.* **90**, 88–103 (2001).
- Liao, J., Wang, Q., Gerya, T. & Ballmer, M. D. Modeling craton destruction by hydration-induced weakening of the upper mantle. *J. Geophys. Res. Solid Earth* **122**, 7449–7466 (2017).
- Faul, U. H. & Jackson, I. The seismological signature of temperature and grain size variations in the upper mantle. *Earth Planet. Sci. Lett.* **234**, 119–134 (2005).
- Ave Lallemand, H. G., Mercier, J. C. C., Carter, N. L. & Ross, J. V. Rheology of the upper mantle—Inferences from peridotite xenoliths. *Tectonophysics* **70**, 85–113 (1980).
- Bernard, R. E., Behr, W. M., Becker, T. W. & Young, D. J. Relationships between olivine CPO and deformation parameters in naturally deformed rocks and implications for mantle seismic anisotropy. *Geochem. Geophys. Geosyst.* **20**, 3469–3494 (2019).
- Dyger, N., Bernard, R. E. & Behr, W. M. Great basin mantle xenoliths record active lithospheric downwelling beneath central Nevada. *Geochem. Geophys. Geosyst.* **20**, 751–772 (2019).

19. Bercovici, D., Ricard, Y. & Richards, M. in *The History and Dynamics of Global Plate Motions* (eds Richards, M. A. et al.) 5–46 (AGU, 2000).
20. Gurnis, M., Zhong, S. & Toth, J. in *The History and Dynamics of Global Plate Motions* (eds Richards, M. A. et al.) 73–94 (AGU, 2000).
21. Behn, M. D., Hirth, G. & Elsenbeck, J. R. Implications of grain size evolution on the seismic structure of the oceanic upper mantle. *Earth Planet. Sci. Lett.* **282**, 178–189 (2009).
22. Braun, J. et al. A simple parameterization of strain localization in the ductile regime due to grain size reduction: a case study for olivine. *J. Geophys. Res. Solid Earth* **104**, 25167–25181 (1999).
23. Hopper, J. R. & Buck, W. R. The initiation of rifting at constant tectonic force—role of diffusion creep. *J. Geophys. Res. Solid Earth* **98**, 16213–16221 (1993).
24. Platt, J. P. & Behr, W. M. Grain size evolution in ductile shear zones: implications for strain localization and the strength of the lithosphere. *J. Struct. Geol.* **33**, 537–550 (2011).
25. Schierjott, J. C., Thielmann, M., Rozel, A. B., Golabek, G. J. & Gerya, T. V. Can grain size reduction initiate transform faults? Insights from a 3-D numerical study. *Tectonics* **39**, TC005793 (2020).
26. Hartz, E. H. & Podladchikov, Y. Y. Toasting the jelly sandwich: the effect of shear heating on lithospheric geotherms and strength. *Geology* **36**, 331–334 (2008).
27. Drury, M. R., Vissers, R. L. M., Vanderwal, D. & Strating, E. H. H. Shear localisation in upper mantle peridotites. *Pure Appl. Geophys.* **137**, 439–460 (1991).
28. Tommasi, A. et al. Structural reactivation in plate tectonics controlled by olivine crystal anisotropy. *Nat. Geosci.* **2**, 422–426 (2009).
29. Bercovici, D. & Ricard, Y. Mechanisms for the generation of plate tectonics by two-phase grain-damage and pinning. *Phys. Earth Planet. Int.* **202**, 27–55 (2012).
30. Bercovici, D. & Ricard, Y. Plate tectonics, damage and inheritance. *Nature* **508**, 513–516 (2014).
31. De Bresser, J. H. P., Ter Heege, J. H. & Spiers, C. J. Grain size reduction by dynamic recrystallization: can it result in major rheological weakening? *Int. J. Earth Sci.* **90**, 28–45 (2001).
32. Karato, S. Grain-growth kinetics in olivine aggregates. *Tectonophysics* **168**, 255–273 (1989).
33. Fuchs, L. & Becker, T. W. Deformation memory in the lithosphere: a comparison of damage-dependent weakening and grain-size sensitive rheologies. *J. Geophys. Res. Solid Earth* **126**, JB020335 (2021).
34. Thielmann, M. & Schmalholz, S. M. Contributions of grain damage, thermal weakening, and necking to slab detachment. *Front. Earth Sci.* **8**, 254 (2020).
35. Dannberg, J. et al. The importance of grain size to mantle dynamics and seismological observations. *Geochem. Geophys. Geosyst.* **18**, 3034–3061 (2017).
36. Gerya, T. V., Bercovici, D. & Becker, T. W. Dynamic slab segmentation due to brittle–ductile damage in the outer rise. *Nature* **599**, 245–250 (2021).
37. Austin, N. & Evans, B. Paleowattmeters: a scaling relation for dynamically recrystallized grain size. *Geology* **35**, 343–346 (2007).
38. Hansen, L. N., Zimmerman, M. E. & Kohlstedt, D. L. Grain boundary sliding in San Carlos olivine: flow law parameters and crystallographic-preferred orientation. *J. Geophys. Res. Solid Earth* **116**, JB008220 (2011).
39. Ohuchi, T. et al. Dislocation-accommodated grain boundary sliding as the major deformation mechanism of olivine in the Earth's upper mantle. *Sci. Adv.* **1**, e1500360 (2015).
40. Hirth, G. & Kohlstedt, D. Water in the oceanic upper mantle: implications for rheology, melt extraction and the evolution of the lithosphere. *Earth Planet. Sci. Lett.* **144**, 93–108 (1996).
41. Jung, H. & Karato, S. I. Effects of water on dynamically recrystallized grain-size of olivine. *J. Struct. Geol.* **23**, 1337–1344 (2001).
42. Saal, A. E., Hauri, E. H., Langmuir, C. H. & Perfit, M. R. Vapour undersaturation in primitive mid-ocean-ridge basalt and the volatile content of Earth's upper mantle. *Nature* **419**, 451–455 (2002).
43. Wang, Q., Bagdassarov, N., Xia, Q. K. & Zhu, B. B. Water contents and electrical conductivity of peridotite xenoliths from the North China Craton: Implications for water distribution in the upper mantle. *Lithos* **189**, 105–126 (2014).
44. Shimizu, I. Theories and applicability of grain size piezometers: the role of dynamic recrystallization mechanisms. *J. Struct. Geol.* **30**, 899–917 (2008).
45. Holtzman, B. K., Chrysochoos, A. & Daridon, L. A thermomechanical framework for analysis of microstructural evolution: application to olivine rocks at high temperature. *J. Geophys. Res. Solid Earth* **123**, 8474–8507 (2018).
46. Speciale, P. A., Behr, W. M., Hirth, G. & Tokle, L. Rates of olivine grain growth during dynamic recrystallization and postdeformation annealing. *J. Geophys. Res. Solid Earth* **125**, JB020415 (2020).
47. Michibayashi, K. & Oohara, T. Olivine fabric evolution in a hydrated ductile shear zone at the Moho Transition Zone, Oman Ophiolite. *Earth Planet. Sci. Lett.* **377**, 299–310 (2013).
48. Kiss, D., Candioti, L. G., Duretz, T. & Schmalholz, S. M. Thermal softening induced subduction initiation at a passive margin. *Geophys. J. Int.* **220**, 2068–2073 (2020).
49. Bird, P., Liu, Z. & Rucker, W. K. Stresses that drive the plates from below: definitions, computational path, model optimization, and error analysis. *J. Geophys. Res. Solid Earth* **113**, JB005460 (2008).
50. Gurnis, M., Hall, C. & Lavier, L. Evolving force balance during incipient subduction. *Geochem. Geophys. Geosyst.* **5**, GC000681 (2004).
51. Katz, R. F., Spiegelman, M. & Langmuir, C. H. A new parameterization of hydrous mantle melting. *Geochem. Geophys. Geosyst.* **4**, GC000681 (2003).
52. van Keken, P. E. & Ballentine, C. J. Dynamical models of mantle volatile evolution and the role of phase transitions and temperature-dependent rheology. *J. Geophys. Res. Solid Earth* **104**, 7137–7151 (1999).
53. Demouchy, S., Tommasi, A., Barou, F., Mainprice, D. & Cordier, P. Deformation of olivine in torsion under hydrous conditions. *Phys. Earth Planet. Int.* **202**, 56–70 (2012).
54. Tielke, J. A., Zimmerman, M. E. & Kohlstedt, D. L. Hydrolytic weakening in olivine single crystals. *J. Geophys. Res. Solid Earth* **122**, 3465–3479 (2017).
55. Behr, W. M. & Hirth, G. Rheological properties of the mantle lid beneath the Mojave region in southern California. *Earth Planet. Sci. Lett.* **393**, 60–72 (2014).
56. Matysiak, A. K. & Trepmann, C. A. The deformation record of olivine in mylonitic peridotites from the Finero Complex, Ivrea Zone: separate deformation cycles during exhumation. *Tectonics* **34**, 2514–2533 (2015).
57. Behr, W. M. & Smith, D. Deformation in the mantle wedge associated with Laramide flat-slab subduction. *Geochem. Geophys. Geosyst.* **17**, 2643–2660 (2016).
58. Precigout, J., Gueydan, F., Gapais, D., Garrido, C. J. & Essaifi, A. Strain localisation in the subcontinental mantle—a ductile alternative to the brittle mantle. *Tectonophysics* **445**, 318–336 (2007).
59. Warren, J. M. & Hirth, G. Grain size sensitive deformation mechanisms in naturally deformed peridotites. *Earth Planet. Sci. Lett.* **248**, 438–450 (2006).
60. Unternehr, P., Peron-Pinvidic, G., Manatschal, G. & Sutra, E. Hyper-extended crust in the South Atlantic: in search of a model. *Pet. Geosci.* **16**, 207–215 (2010).
61. Péron-Pinvidic, G. & Manatschal, G. From microcontinents to extensional allochthons: witnesses of how continents rift and break apart? *Pet. Geosci.* **16**, 189–197 (2010).
62. Huisman, R. S. & Beaumont, C. Symmetric and asymmetric lithospheric extension: relative effects of frictional-plastic and viscous strain softening. *J. Geophys. Res. Solid Earth* **108**, JB002026 (2003).
63. Lavier, L. L. & Manatschal, G. A mechanism to thin the continental lithosphere at magma-poor margins. *Nature* **440**, 324–328 (2006).
64. Buck, W. R., Lavier, L. L. & Poliakov, A. N. B. Modes of faulting at mid-ocean ridges. *Nature* **434**, 719–723 (2005).

Publisher's note Springer Nature remains neutral with regard to jurisdictional claims in published maps and institutional affiliations.



Open Access This article is licensed under a Creative Commons Attribution 4.0 International License, which permits use, sharing, adaptation, distribution and reproduction in any medium or format, as long as you give appropriate credit to the original author(s) and the source, provide a link to the Creative Commons license, and indicate if changes were made. The images or other third party material in this article are included in the article's Creative Commons license, unless indicated otherwise in a credit line to the material. If material is not included in the article's Creative Commons license and your intended use is not permitted by statutory regulation or exceeds the permitted use, you will need to obtain permission directly from the copyright holder. To view a copy of this license, visit <http://creativecommons.org/licenses/by/4.0/>.

© The Author(s) 2022

Methods

Numerical experiments were conducted with a finite-difference thermo-mechanical numerical code with a fully staggered Eulerian grid and a Lagrangian particle field based on the marker-in-cell technique^{65–67}. The mechanical implementation employs a visco-elasto-plastic rheology, and governing equations are discretized on the non-deformable Eulerian grid and solved with MATLAB's backslash direct solver for the two velocity components and dynamic pressure. Temperature is solved separately on the Eulerian pressure nodes with MATLAB's backslash direct solver. Material properties are interpolated on freely moving Lagrangian markers that advect through the fixed Eulerian grid according to a fourth-order Runge–Kutta derived velocity field.

Governing equations. The mechanical model implements the equations for conservation of mass (incompressible)

$$\frac{\partial u_i}{\partial x_i} = 0 \quad (1)$$

and conservation of momentum (Stokes equation)

$$-\frac{\partial P}{\partial x_i} + \frac{\partial \tau_{ij}}{\partial x_j} = \rho g_i \quad (2)$$

where P is mean stress, u_i is velocities, x_i is spatial coordinates, τ_{ij} is deviatoric stress tensor, ρ is density and g_i is the gravitational acceleration.

Temperature is implemented by the energy equation

$$\rho C_p \left(\frac{DT}{Dt} \right) = k \frac{\partial^2 T}{\partial x_i^2} + H_a + H_r + H_s \quad (3)$$

where T is temperature, t is time, C_p is isobaric heat capacity and k is thermal conductivity coefficient. Additional heat sources include adiabatic heating (H_a), radioactive heating (H_r) and shear heating (H_s):

$$H_a = \alpha T \left(\frac{DP}{Dt} \right) \quad (4)$$

$$H_s = \xi \sigma_{ij} \dot{\epsilon}_{ij} \quad (5)$$

where ξ is fraction of work adding to shear heating. H_r is implemented as a constant for each rock type. Density changes related to thermal expansion α and compressibility β are implemented following

$$\rho = \rho_r [1 + \beta (P - P_r)] \times [1 - \alpha (T - T_r)] \quad (6)$$

where ρ_r is reference density, P_r is reference pressure (1 bar), T_r is reference temperature (273 K), α is thermal expansivity and β is compressibility.

Rheological model. The visco-elastic relation between stress and strain rate follows a Maxwell-type model composed of a viscous and an elastic strain rate part

$$\dot{\epsilon}_{ij} = \frac{1}{2} \tau_{ij} + \frac{1}{2G} \frac{D\tau_{ij}}{Dt} \quad (7)$$

where G indicates the shear modulus and η the effective viscosity with lower and upper cut-offs of 10^{17} and 10^{25} Pa s, respectively. Elasticity is implemented by adapting the effective viscosity depending on the 'computational' time step and the stress history^{65,68,69}. The objective co-rotational time derivative of visco-elastic stresses is discretized as a function after applying first-order finite difference

$$\frac{D\tau_{ij}}{Dt} = \frac{\tau_{ij} - \tau_{ij}^{\text{old}}}{\Delta t} \quad (8)$$

with

$$\tau_{ij} = 2\dot{\epsilon}_{ij}Z + \tau_{ij}^{\text{old}}(1 - Z) \quad (9)$$

and the visco-elasticity factor

$$Z = \frac{\Delta t \times \Delta G}{\eta + \Delta t \times \Delta G} \quad (10)$$

with η as effective viscosity, which leads to the numerical visco-elastic viscosity

$$\eta_{\text{num}} = \eta \times Z = \frac{\eta \times \Delta t \times G}{\eta + \Delta t \times G} \quad (11)$$

used to solve the set of equations.

The viscous strain rate is composed of both dislocation and diffusion creep following the general power law for a viscous implementation¹:

$$\dot{\epsilon} = A_D \times fH_2O^r \times \sigma^n \times d^m \times \exp\left(-\frac{E + P \times V}{RT}\right), \quad (12)$$

where A_D is pre-exponent, fH_2O is water fugacity, r is water-fugacity exponent, σ is stress, n is stress exponent, d is grain size, m is grain-size exponent, E is activation energy, V is activation volume and R is gas constant ($8.314 \text{ J K}^{-1} \text{ mol}^{-1}$).

Viscosities for dislocation creep η_{disl} and diffusion creep η_{diff} are calculated separately by reformulating the general viscous power law (equation (12)):

$$\eta_{\text{disl,diff}} = 0.5 \times \frac{1}{A_D fH_2O^r} \times \sigma_{\text{II}}^{(1-n)} \times d^{-m} \times \exp\left(\frac{E + PV}{RT}\right) \quad (13)$$

with

$$\sigma_{\text{II}} = \sqrt{\frac{1}{2} \tau_{ij}^2} \quad (14)$$

The composite viscosity resulting for the simultaneous occurrence of dislocation and diffusion creep follows

$$\eta_v = \left(\frac{1}{\eta_{\text{disl}}} + \frac{1}{\eta_{\text{diff}}} \right)^{-1} \quad (15)$$

Extended Data Fig. 1 shows vertical viscosity (Extended Data Fig. 1a–c) and strength profiles (Extended Data Fig. 1d–f) for variable grain sizes, strain rates and hydrogen concentrations. Such an illustration helps interpret the dominating deformation mechanism in the uppermost mantle depending on the investigated variables.

Plastic failure occurs if the visco-elastic differential trial stresses exceed the yield stress ($F > 0$) according to the Drucker–Prager yield criterion with a flow potential resulting in a dilation angle of zero:

$$F = \sigma_{\text{II}} - \sigma_y \quad (16)$$

where

$$\sigma_y = P \times (1 - \lambda_f) \times \sin \varphi + C \times \cos \varphi \quad (17)$$

where C is cohesion, φ is friction angle and λ_f is fluid pressure ratio. Exceeded stresses are kept within the failure envelope by decreasing the plastic viscosity η_p to maintain those stresses

$$\eta_p = \frac{\sigma_y}{2\dot{\epsilon}_{\text{II}}} \quad (18)$$

where

$$\dot{\epsilon}_{\text{II}} = \sqrt{\frac{1}{2} \dot{\epsilon}_{ij}^2} \quad (19)$$

The effective viscosity going into the viscous part of the Maxwell rheological model follows

$$\eta = \min(\eta_v, \eta_p) \quad (20)$$

After interpolation of the Eulerian velocity field onto the Lagrangian markers, stress changes and plasticity are calculated on those. The updated effective viscosity is then interpolated back onto the Eulerian nodes and used to solve the system of equations. Time steps exhibit maximally $\leq 1,000$ yr following a Courant number of 0.25.

Grain-size-evolution model. Grain size is calculated on the basis of the palaeo-wattmeter⁷⁷, in contrast to grain-size pinning and damage in a two-phase medium. Grain size depends on independently acting growth and reduction terms^{29,36} (see ref. ³³ for a comparison). Grain-size reduction rate is related to mechanical work executed by dislocation creep ($\sigma \dot{\epsilon}_{\text{disl}}$) and is described by

$$\dot{d}_{\text{red}} = \frac{\sigma \dot{\epsilon}_{\text{disl}} \lambda d^2}{c\gamma}, \quad (21)$$

where σ is stress, $\dot{\epsilon}_{\text{disl}}$ is dislocation-creep strain rate, c is a geometric constant (π for spheric grains), γ is the grain boundary energy (1.4 J m^{-2} for olivine⁷⁰) and λ denotes the fraction of work that goes into grain-size reduction ($\lambda = 1 - \xi$), whereas the rest of the work goes into the shear heating term (H_s ; see equation (5))^{71–73}. Fitting experimentally derived olivine grain sizes versus expected grain size using the palaeo-wattmeter with the grain-growth law constrained by ref. ⁴⁶ and others resulted in a λ of 0.01 (Extended Data Fig. 3a). The constrained fraction of work that adds to the grain-size reduction term is substantially smaller than previously applied fractions of $\lambda = 0.1$ (refs. ^{21,35,37}). However, a recent study demonstrated that

the energy partitioning factor λ of olivine ranges between 0.003 and 0.040 for a wide spectrum of pressure and temperature conditions⁴⁵ (Extended Data Fig. 5).

Grain-growth rate follows a normal relationship given by

$$\dot{d}_{\text{gr}} = K_{\text{g}} f_{\text{H}_2\text{O}} \exp\left(-\frac{E_{\text{g}} + P \times V_{\text{g}}}{RT}\right) p^{-1} d^{1-p}, \quad (22)$$

where K_{g} is growth-rate constant, $f_{\text{H}_2\text{O}}$ is water fugacity, E_{g} is activation energy, V_{g} is activation volume, P is pressure, T is temperature, R is gas constant, d is grain size and p is growth exponent. We applied experimentally derived olivine grain-growth parameters by ref. ⁴⁶ and others that result in significantly slower grain growth than previous constraints³² (Extended Data Figs. 3b and 6). The new grain size d_{new} is calculated on the Lagrangian markers following

$$d_{\text{new}} = \left(\dot{d}_{\text{gr}} - \dot{d}_{\text{red}}\right) \times Dt \quad (23)$$

and then goes into the power-law creep calculation for diffusion creep (equation (13)).

Model set-up. The Eulerian model domain measures 1,000 × 670 km in x and y directions, respectively (Extended Data Fig. 2). The nodal resolution is 501 × 336 in x and y directions, which results in a cell size of 2 × 2 km. Rock type, rheological information and mechanical, thermal and grain-size material properties (Extended Data Tables 1–4) are stored on 25 Lagrangian markers per Eulerian cell. The initial marker distribution (Extended Data Fig. 3) describes, from top to bottom, (1) a 10-km-thick layer of low-viscosity sticky air, which allows for a quasi-stress-free surface (air–rock interface)⁷⁴, (2) a 23-km-thick upper continental crust with quartzite rheology^{75,76}, (3) a 10-km-thick lower continental crust with anorthite rheology⁴ and (4) 627 km of upper mantle with dry or wet olivine rheology¹. Although no olivine occurs below 410 km depth (transition to wadsleyite, ringwoodite and majorite), olivine rheology is implemented here for the entire upper mantle for simplification and due to the lack of respective flow laws. A weak inclusion of 4 × 4 km of quartzite rheology is placed in the lower continental crust at $x = 500$ km to localize rifting at the centre of the model (Extended Data Fig. 2).

Fugacity in the upper continental crust is calculated after ref. ⁷⁶. In the upper mantle, fugacity is implemented as constant hydrogen concentration obtained and constrained following the Paterson calibration⁷⁷ with values of $C_{\text{OH}} = 50, 175, 600$ or $2,500 \text{ H}/10^6 \text{ Si}$, covering the range of estimated values obtained from experimental studies^{40,41} as well as measurements from mid-ocean-ridge basalts^{42,78} and peridotite xenoliths⁴³, which affects both viscosity (equation (13)) and grain growth (equation (22)). Elevated hydrogen concentrations in the upper mantle are introduced due to dehydration of subducting slabs or released from the mantle transition zone⁷⁹.

The initial temperature distribution describes 0 °C within the sticky-air layer, a linear increase from 0 °C at the surface ($y = 10$ km) to 660 °C at the Moho ($y = 43$ km), and from there to 1,345 °C at the thermally induced LAB at 150 km depth ($y = 160$ km). Below the LAB, a static temperature increase of 0.5 °C km⁻¹ is introduced. Such a temperature distribution is in agreement with the thermal structure of the lithosphere below continents⁸⁰.

Oceanic crust with an anorthite–diopside (50/50) rheology⁸¹ is produced if mantle rock markers less than 8 km below the surface (air–rock interface) have a temperature of <400 °C.

Boundary conditions. Lateral boundaries prescribe a constant horizontal velocity of $v_x = -0.5 \text{ cm yr}^{-1}$ on the left and $v_x = 0.5 \text{ cm yr}^{-1}$ on the right side (Extended Data Fig. 1). In addition, experiments with a total horizontal divergence of 4 and 8 cm yr⁻¹ were conducted (Extended Data Fig. 6c,d). Vertical velocities at lateral boundaries prescribe a free-slip condition (zero shear stress). Top and bottom boundaries exhibit vertical velocities to ensure conservation of area during divergence (Extended Data Fig. 1) and horizontal velocities prescribing free slip.

Initial grain-size distribution. Grain sizes in the crust remain constant at 1 mm. Initial grain size in the mantle of all experiments in the main figures logarithmically increases from 5 mm at the Moho to 10 cm at the LAB and 10 cm throughout the lower part of the mantle. Extended Data Fig. 3 shows the grain-size distribution within the uppermost 300 km after 10 Myr (Extended Data Fig. 3a) and the temporal evolution of average grain size between 200 and 410 km depth (Extended Data Fig. 3b) for different initial conditions. Grain sizes within the lithosphere are driven mainly by the reduction term due to lower temperatures. High temperatures and thus fast growth rates allow the lower part of the model domain to rapidly restore deformation-related reduced grain sizes. As a result, the initial grain size within the lower 300 km of the model is of little importance, while initial grain sizes should be large enough throughout the lithosphere not to be dependent on initial growth.

Surface-evolution model. The surface line (rock–air interface) undergoes simple syn-tectonic sedimentation and erosion mimicked by a linear diffusion scheme

$$\frac{\partial h_s}{\partial t} = \kappa \frac{\partial^2 h_s}{\partial x_s^2}, \quad (24)$$

where h is surface elevation and κ is diffusion coefficient ($10^{-6} \text{ m}^2 \text{ s}^{-1}$). Syn-tectonic sediments have equal material and strength properties as the initial sediment sequence.

Data availability

All input files used in the numerical modelling are available at <https://doi.org/10.3929/ethz-b-000545342>⁸².

Code availability

The C and Matlab codes used for numerical experiments and visualization are available at <https://doi.org/10.3929/ethz-b-000545342>⁸².

References

- Gerya, T. *Introduction to Numerical Geodynamic Modelling* (Cambridge Univ. Press, 2010).
- Ruh, J. B. Numerical modeling of tectonic underplating in accretionary wedge systems. *Geosphere* **16**, 1385–1407 (2020).
- Ruh, J. B. & Vergés, J. Effects of reactivated extensional basement faults on structural evolution of fold-and-thrust belts: insights from numerical modelling applied to the Kopet Dagh Mountains. *Tectonophysics* **746**, 493–511 (2018).
- Moresi, L., Dufour, F. & Mühlhaus, H. B. A Lagrangian integration point finite element method for large deformation modeling of viscoelastic geomaterials. *J. Comput. Phys.* **184**, 476–497 (2003).
- Moresi, L. et al. Computational approaches to studying non-linear dynamics of the crust and mantle. *Phys. Earth Planet. Int.* **163**, 69–82 (2007).
- Duyster, J. & Stockhert, B. Grain boundary energies in olivine derived from natural microstructures. *Contrib. Mineral. Petrol.* **140**, 567–576 (2001).
- Austin, N. & Evans, B. The kinetics of microstructural evolution during deformation of calcite. *J. Geophys. Res. Solid Earth* **114**, JB006138 (2009).
- Poliak, E. I. & Jonas, J. J. A one-parameter approach to determining the critical conditions for the initiation of dynamic recrystallization. *Acta Mater.* **44**, 127–136 (1996).
- Rosakis, P., Rosakis, A. J., Ravichandran, G. & Hodowany, J. A thermodynamic internal variable model for the partition of plastic work into heat and stored energy in metals. *J. Mech. Phys. Solids* **48**, 581–607 (2000).
- Crameri, F. et al. A comparison of numerical surface topography calculations in geodynamic modelling: an evaluation of the ‘sticky air’ method. *Geophys. J. Int.* **189**, 38–54 (2012).
- Brodie, K. H. & Rutter, E. H. Deformation mechanisms and rheology: why marble is weaker than quartzite. *J. Geol. Soc. Lond.* **157**, 1093–1096 (2000).
- Shinevar, W. J., Behn, M. D. & Hirth, G. Compositional dependence of lower crustal viscosity. *Geophys. Res. Lett.* **42**, 8333–8340 (2015).
- Paterson, M. S. The determination of hydroxyl by infrared-absorption in quartz, silicate glasses and similar materials. *Bull. Mineral.* **105**, 20–29 (1982).
- Dixon, J. E., Leist, L., Langmuir, C. & Schilling, J. G. Recycled dehydrated lithosphere observed in plume-influenced mid-ocean-ridge basalt. *Nature* **420**, 385–389 (2002).
- Hirschmann, M. M. Water, melting, and the deep Earth H₂O cycle. *Annu. Rev. Earth Planet. Sci.* **34**, 629–653 (2006).
- Goes, S., Hasterok, D., Schutt, D. L. & Klocking, M. Continental lithospheric temperatures: a review. *Phys. Earth Planet. Int.* **306**, 106509 (2020).
- Dimanov, A. & Dresen, G. Rheology of synthetic anorthite–diopside aggregates: implications for ductile shear zones. *J. Geophys. Res. Solid Earth* **110**, JB003431 (2005).
- Ruh, J. B. Grain size evolution controls on lithospheric weakening during rifting. *ETH Research Collection* <https://doi.org/10.3929/ethz-b-000545342> (2021).
- Van der Wal, D., Chopra, P., Drury, M. & Fitz Gerald, J. D. Relationships between dynamically recrystallized grain size and deformation conditions in experimentally deformed olivine rocks. *Geophys. Res. Lett.* **20**, 1479–1482 (1993).

Acknowledgements

The authors received no specific funding for this work.

Author contributions

All authors made substantial contribution to the work. J.B.R. developed the numerical code, conducted the experiments and wrote the manuscript. L.T. investigated experimental data to infer crucial parameters, interpreted the data and revised the manuscript. W.M.B. contributed to the conception and design of the study and substantially revised it.

Competing interests

The authors declare no competing interests.

Additional information

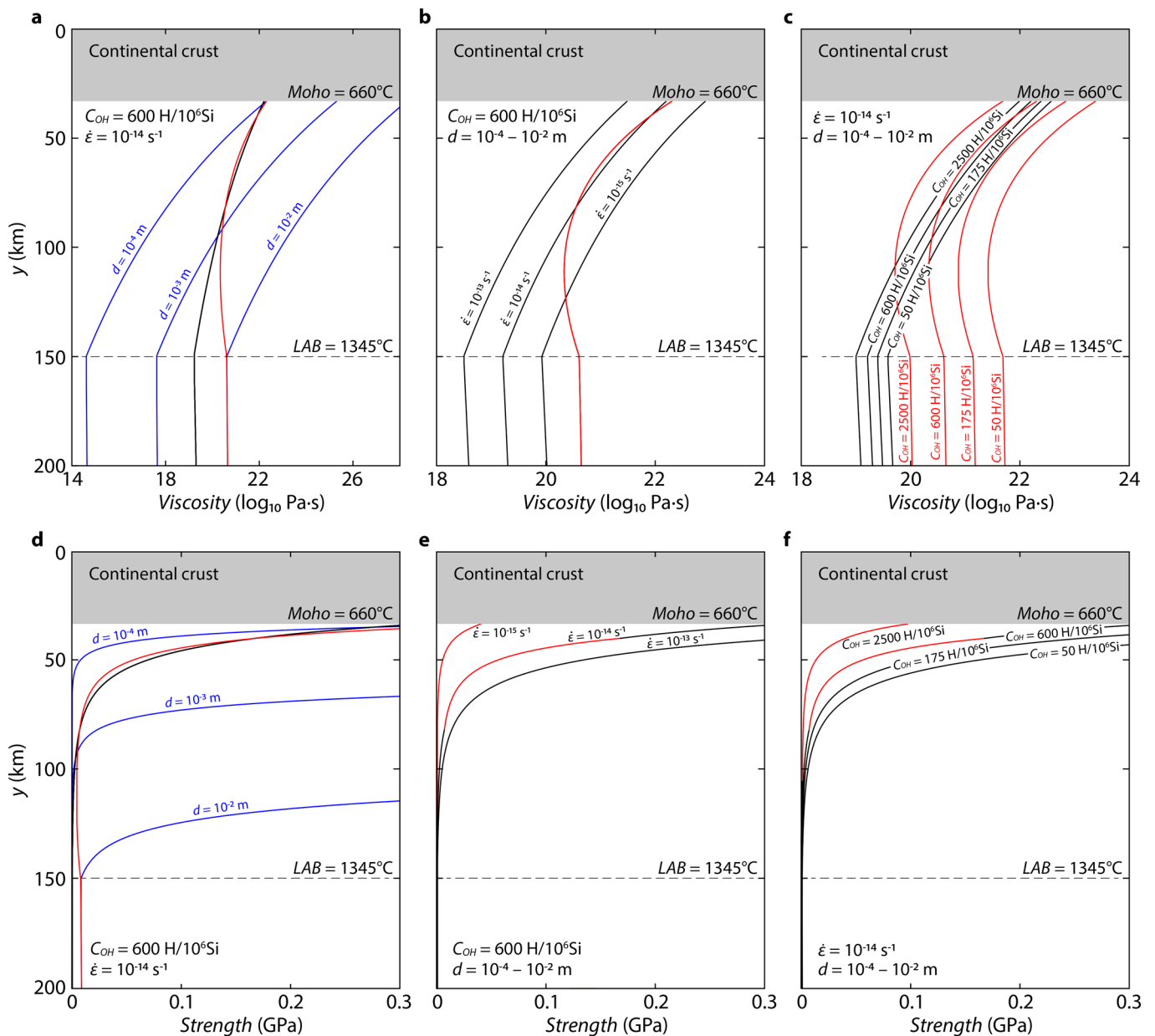
Extended data is available for this paper at <https://doi.org/10.1038/s41561-022-00964-9>.

Supplementary information The online version contains supplementary material available at <https://doi.org/10.1038/s41561-022-00964-9>.

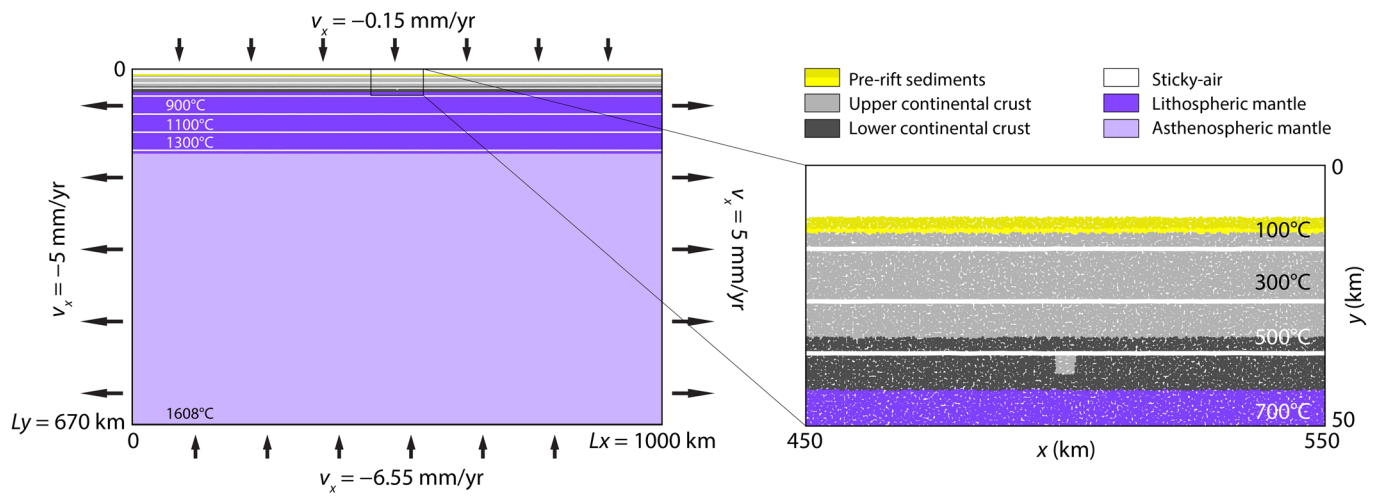
Correspondence and requests for materials should be addressed to J. B. Ruh.

Peer review information *Nature Geoscience* thanks Sylvie Demouchy and the other, anonymous, reviewer(s) for their contribution to the peer review of this work. Primary Handling Editors: Louise Hawkins and James Super, in collaboration with the *Nature Geoscience* team.

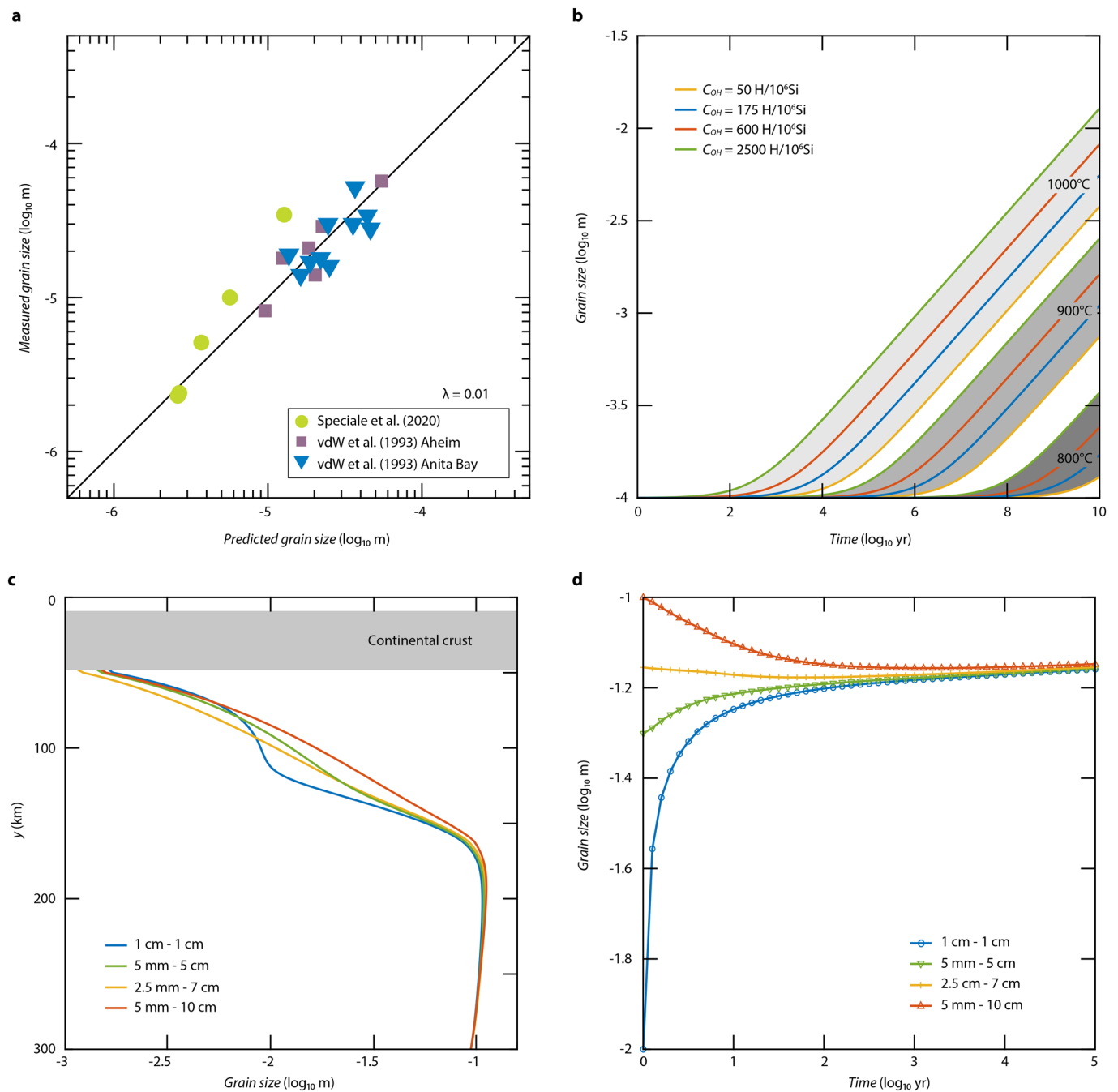
Reprints and permissions information is available at www.nature.com/reprints.



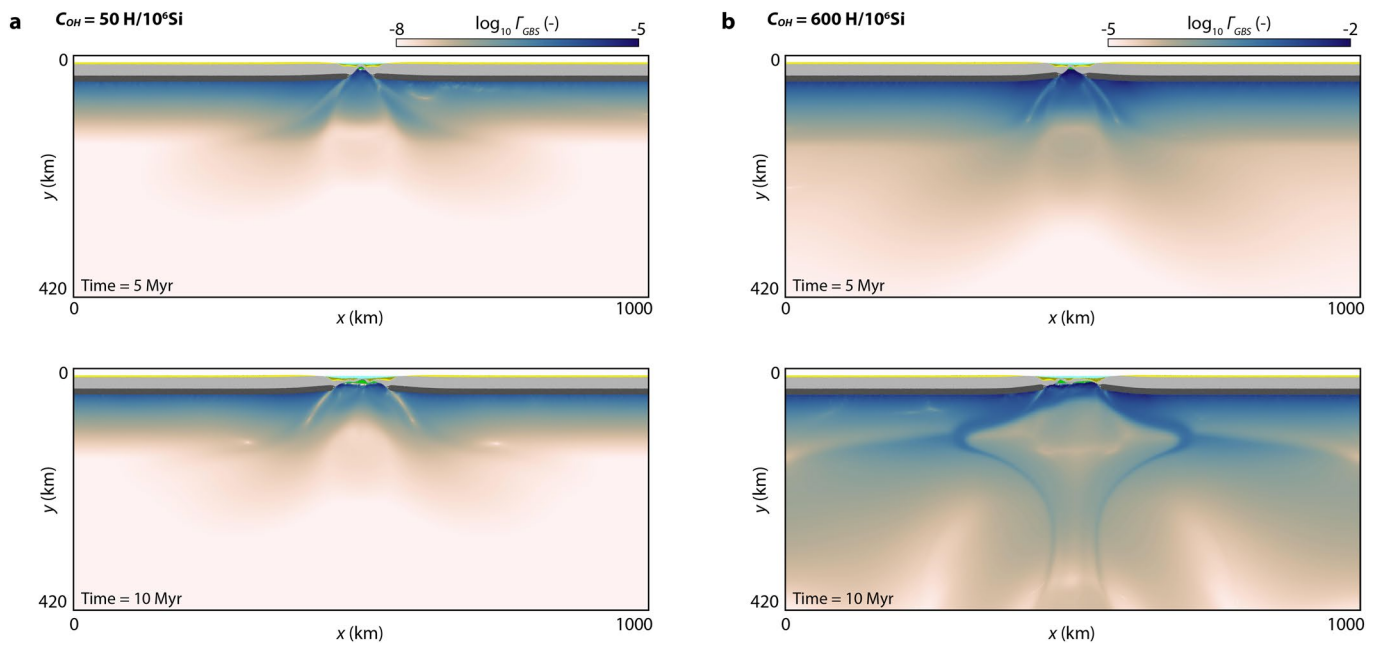
Extended Data Fig. 1 | Lithospheric strength and viscosity profiles. Viscosity (a-c) and strength (d-f) profiles calculated by dislocation and diffusion creep flow parameters given in Extended Data Table 1 for variable grain size (a, d), strain rate (b, e), and hydrogen concentration (c, f). Black: Dislocation creep. Blue: Diffusion creep, constant grain size. Red: Diffusion creep, variable grain size between Moho and LAB (10^{-4} – 10^{-2} m). Color in (e) and (f) show which deformation mechanism is defining the strength.



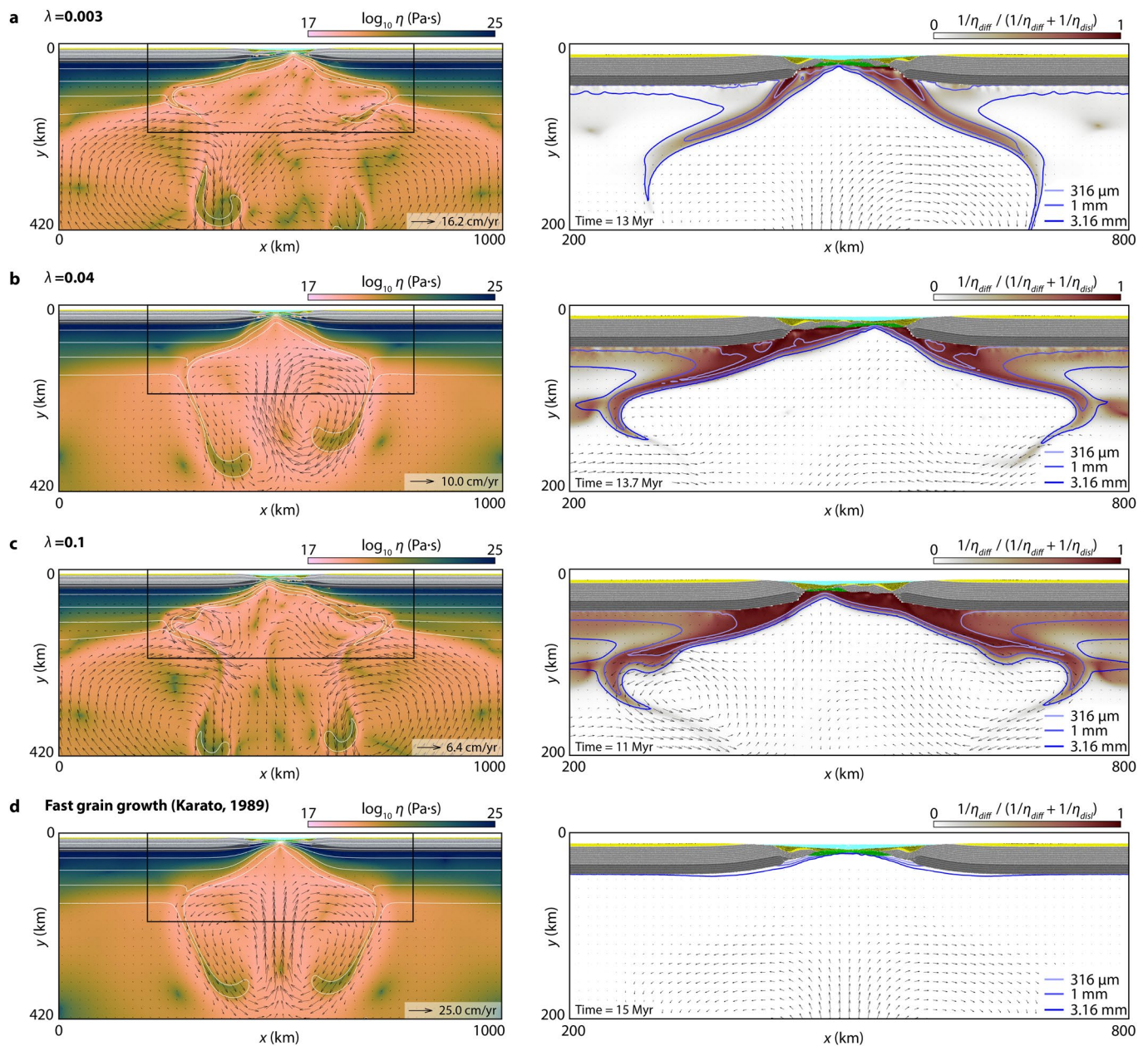
Extended Data Fig. 2 | Model setup. Colors represent initial marker distribution. Arrows indicate velocity boundary conditions. White lines show initial temperature distribution in the lithosphere.



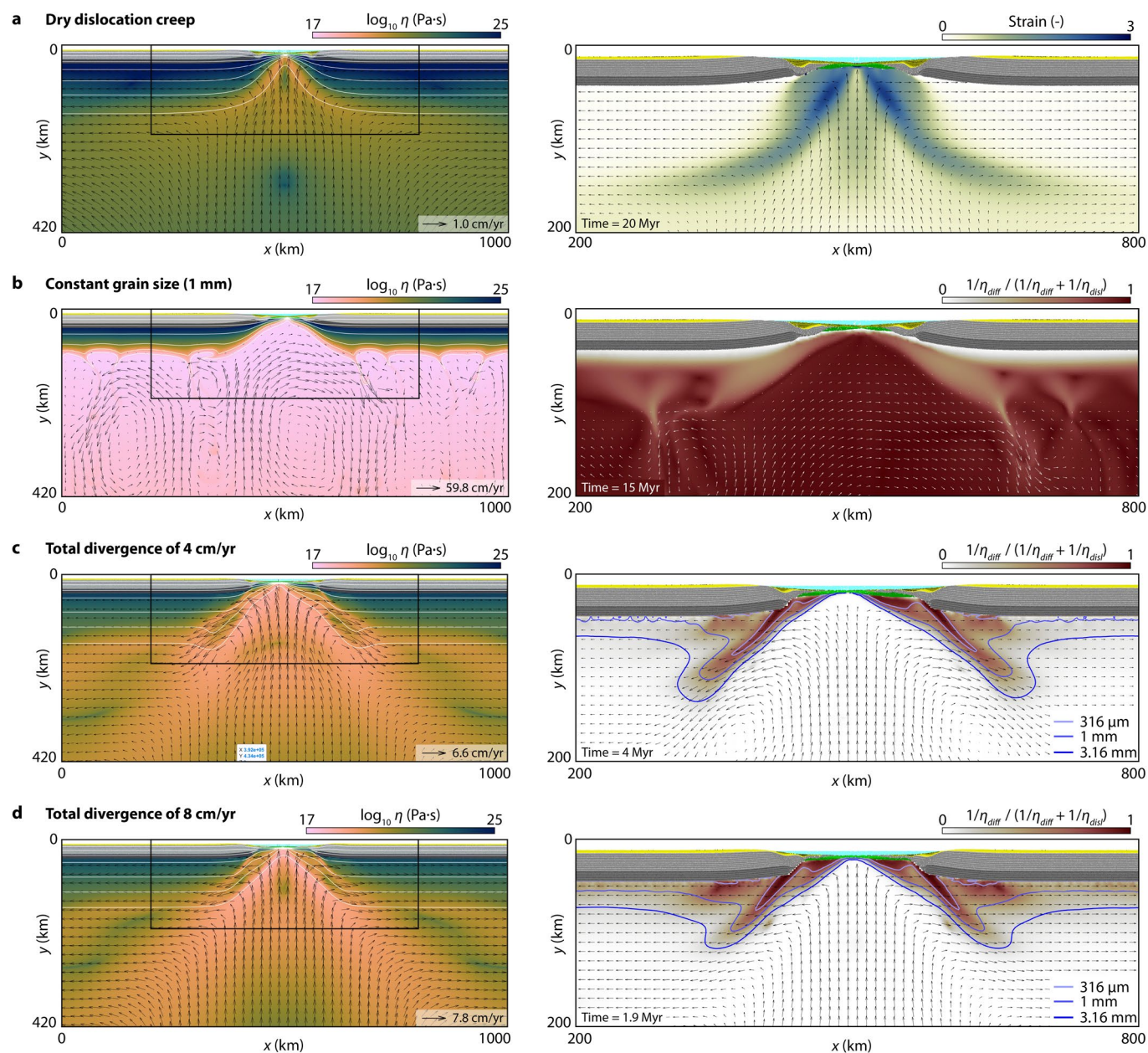
Extended Data Fig. 3 | (a) Fitting of experimentally measured and predicted olivine grain size, resulting in a $\lambda = 0.01^{83}$. (b) Predicted grain growth with parameters from Speciale, et al.⁴⁶ and an initial grain size of 10^{-4} m for different hydrogen concentrations at 800, 900, and 1000 °C. (c, d) Testing variable initial grain size distributions. (c) Profiles of grain size after 10 Myr between $x = 10$ –100 km, where shear zone effects are absent. Blue: Constant initial grain size of 1 cm. Green: 5 mm at Moho to 5 cm at LAB. Yellow: 2.5 mm at Moho to 7 cm at LAB. Red: 5 mm at Moho to 10 cm at LAB. (d) Temporal evolution of average grain size between 200 to 410 km of the upper mantle. Blue: Initial grain size in lower part of upper mantle of 1 cm. Green: Initial grain size in lower part of upper mantle of 5 cm. Yellow: Initial grain size in lower part of upper mantle of 7 cm. Red: Initial grain size in lower part of upper mantle of 10 cm.



Extended Data Fig. 4 | Effect of grain boundary sliding (GBS) on upper mantle dynamics. Colors indicate the percentage of GBS strain rate relative to the total strain rate for the upper mantle: $\Gamma_{GBS} = \dot{\epsilon}_{GBS} / (\dot{\epsilon}_{GBS} + \dot{\epsilon}_{disl} + \dot{\epsilon}_{diff})$. **(a)** $C_{OH} = 50 \text{ H}/10^6 \text{ Si}$. **(b)** $C_{OH} = 600 \text{ H}/10^6 \text{ Si}$. The GBS flow law by Ohuchi et al.³⁹ follows $\dot{\epsilon}_{GBS} = A_{GBS} f_{H_2O}^{r_{GBS}} \frac{\sigma^n}{d} \exp\left(-\frac{E_{GBS} + V_{GBS}P}{RT}\right)$, with $A_{GBS} = 10^{-4.98} \text{ MPa}^{-n}$, $n_{GBS} = 3$, $r_{GBS} = 1.25$, $E_{GBS} = 423 \text{ kJ}$, and $V_{GBS} = 17.6 \text{ cm}^3/\text{mol}$.



Extended Data Fig. 5 | Additional experiments with variable grain-size-evolution parameters. Viscosity of upper mantle, marker composition of crust and deformation mechanism (red: diffusion creep, white: dislocation creep) of experiments with $C_{OH} = 600 \text{ H}/10^6 \text{ Si}$ and additional grain size parameters. White lines denote isotherms up to 1300 °C. Blue contours indicate grain size. Grey and yellow colors: Continental crust marker composition. Green: Oceanic crust marker composition. **(a)** $\lambda = 0.003$. **(b)** $\lambda = 0.04$. **(c)** $\lambda = 0.1$. **(d)** Grain growth parameter from Karato³².



Extended Data Fig. 6 | Additional experiments with variable rheology, constant grain size and faster divergence rates. (a) Viscosity of upper mantle, marker composition of crust and accumulated viscous strain of experiments with pure dry dislocation creep mantle rheology. White lines denote isotherms up to 1300 °C. (b-d) Viscosity of upper mantle, marker composition of crust and deformation mechanism (red: diffusion creep, white: dislocation creep) of experiments with $C_{OH} = 600 \text{ H}/10^6\text{Si}$. a) Constant grain size of 1 mm. b) Total divergence rate of 4 cm yr^{-1} . c) Total divergence rate of 8 cm yr^{-1} . White lines denote isotherms up to 1300 °C. Blue contours indicate grain size. Grey and yellow colors: Continental crust marker composition. Green: Oceanic crust marker composition.

Extended Data Table 1 | Material parameters

Rock type	ρ_r (kg/m ³)	G (GPa)	ϕ (°)†	C (MPa)†	λ_f (-)
Sticky-air	1	100	-	-	-
Sediments	2500	100	30 (15)	10 (1)	0.7
Upper continental crust	2700	100	30 (15)	25 (1)	0.4
Lower continental crust	2800	100	30 (15)	25 (1)	0
Oceanic crust	3000	100	30 (15)	25 (1)	0
Upper mantle	3300	100	30	25 (10)	0

† Values in brackets indicate strain weakened value

Extended Data Table 2 | Flow law parameters

Rock type	Deformation mode	A_0 ($\text{Pa}^{-n} \cdot \text{s}$)	n (-)	m (-)	$f_{\text{H}_2\text{O}}$ (Pa)*	r (-)	Q (kJ/mol)	Reference
Sticky-air	linear	$5 \cdot 10^{-18}$	1	-	-	-	-	Crameri et al., 2012
Sediments (quartzite)	dislocation	$6.31 \cdot 10^{-36}$	4	0	$5521 \cdot 10^6 \cdot \exp(-(31.28 \cdot 10^{-3} - 2.009 \cdot 10^{-5} \cdot P)/(R \cdot T))$	1	135	Hirth et al., 2001
	diffusion	$6.31 \cdot 10^{-19}$	1	2	-	-	220	Brodie and Rutter, 2000
Upper continental crust (quartzite)	dislocation	$6.31 \cdot 10^{-36}$	4	0	$5521 \cdot 10^6 \cdot \exp(-(31.28 \cdot 10^{-3} - 2.009 \cdot 10^{-5} \cdot P)/(R \cdot T))$	1	135	Hirth et al., 2001;
	diffusion	$6.31 \cdot 10^{-19}$	1	2	-	-	220	Brodie and Rutter, 2000
Lower continental crust (anorthite)	dislocation	$5.01 \cdot 10^{-12}$	3	0	-	-	648	Rybacki and Dresen, 2000
	diffusion	$1.26 \cdot 10^{-12}$	1	3	-	-	467	Rybacki and Dresen, 2000
Oceanic crust (anorthite-diopsid 50/50)	dislocation	$2.14 \cdot 10^{-16}$	4.1	0	-	-	723	Dimanov and Dresen, 2005
	diffusion	$1.21 \cdot 10^{-19}$	1	3	-	-	436	Dimanov and Dresen, 2005
Dry upper mantle (olivine)	dislocation	$1.1 \cdot 10^{-16}$	3.5	0	-	-	$530 + 17 \cdot 10^{-6} \cdot P$	Hirth and Kohlstedt, 2003
	diffusion	$1.5 \cdot 10^{-15}$	1	3	-	-	$375 + 6 \cdot 10^{-6} \cdot P$	Hirth and Kohlstedt, 2003
Wet upper mantle (olivine)	dislocation	$9 \cdot 10^{-20}$	3.5	0	C_{OH}	1.2	$480 + 11 \cdot 10^{-6} \cdot P$	Hirth and Kohlstedt, 2003
	diffusion	$1 \cdot 10^{-27}$	1	3	C_{OH}	1	$335 + 4 \cdot 10^{-6} \cdot P$	Hirth and Kohlstedt, 2003

*Water fugacity after Shinevar et al. (2015); $C_{\text{OH}} = 50, 175, 600, 2500 \text{ H}/10^6 \text{ Si}$

Extended Data Table 3 | Thermal parameters

Rock type	C_p (kg/m ³)	k (W/m/K)	α (1/K)	β (1/Pa)	H_r (-)
Olivine	$3 \cdot 10^6$	200	0	-	-
Sediments	1000	2.5	$2 \cdot 10^{-5}$	$4.5 \cdot 10^{-12}$	$2 \cdot 10^{-6}$
Upper continental crust	1000	2	$2 \cdot 10^{-5}$	$4.5 \cdot 10^{-12}$	$2 \cdot 10^{-6}$
Lower continental crust	1000	1.6	$2 \cdot 10^{-5}$	$4.5 \cdot 10^{-12}$	$2 \cdot 10^{-7}$
Oceanic crust	1000	2	$2 \cdot 10^{-5}$	$4.5 \cdot 10^{-12}$	$2 \cdot 10^{-7}$
Upper mantle	1000	1.6	$2 \cdot 10^{-5}$	$4.5 \cdot 10^{-12}$	$2 \cdot 10^{-8}$

C_p = Heat capacity

k = Thermal conductivity

α = Thermal expansivity

β = Compressibility

H_r = Radioactive heating

Extended Data Table 4 | Grain size evolution parameters

Rock type	Upper mantle (olivine)	Reference
<i>Reduction parameters</i>		
c (-)	3.1415	Austin and Evans, 2007
γ (J/m ²)	1.4	Duyster and Stöckert, 2001
λ (-)	0.01	this study
<i>Growth parameters</i>		
K_g (m ^p /s)*	3	Speciale et al., 2020
p (-)	3.2	Speciale et al., 2020
f H ₂ O (Pa)†	C_{OH}	Hirth and Kohlstedt, 1996
E_g (kJ/mol)	620	Speciale et al., 2020
V_g (m ³ /mol)	$5 \cdot 10^{-6}$	Speciale et al., 2020

*Value adapted for reference model with $C_{OH} = 600 \text{ H}/10^6 \text{ Si}$

† $C_{OH} = 50, 175, 600, 2500 \text{ H}/10^6 \text{ Si}$